

Multi-View Industrial Anomaly Detection with Epipolar Constrained Cross-View Fusion

Yifan Liu^{1,2} Xun Xu¹ Shijie Li¹ Jingyi Liao¹ Xulei Yang¹

¹ Institute for Infocomm Research (I²R), A*STAR, Singapore

² National University of Singapore

Abstract

Multi-camera systems provide richer contextual information for industrial anomaly detection. However, traditional methods process each view independently, disregarding the complementary information across viewpoints. Existing multi-view anomaly detection approaches typically employ data-driven cross-view attention for feature fusion but fail to leverage the unique geometric properties of multi-camera setups. In this work, we introduce an epipolar geometry-constrained attention module to guide cross-view fusion, ensuring more effective information aggregation. To further enhance the potential of cross-view attention, we propose a pretraining strategy inspired by memory bank-based anomaly detection. This approach encourages normal feature representations to form multiple local clusters and incorporate multi-view aware negative sample synthesis to regularize pretraining. We demonstrate that our epipolar guided multi-view anomaly detection framework outperforms existing methods on the state-of-the-art multi-view anomaly detection dataset.

1. Introduction

Detecting defects is crucial for quality assurance in industrial processes [1, 2]. Due to the diverse and unconstrained nature of defects, this task is often formulated as unsupervised anomaly detection. The advancement of industrial anomaly detection has been largely driven by the introduction of diverse and realistic datasets [3, 4]. However, most existing methods focus on analyzing defects from a single snapshot of an object. In practical industrial settings, production lines are often equipped with multiple cameras, capturing objects from different viewpoints. This setup has led to the emergence of studies in multi-view industrial anomaly detection (MVIAD) [5].

Despite the advantages of multi-view observations, existing approaches often fail to fully exploit cross-view relationships [5]. A common strategy is to train separate mod-

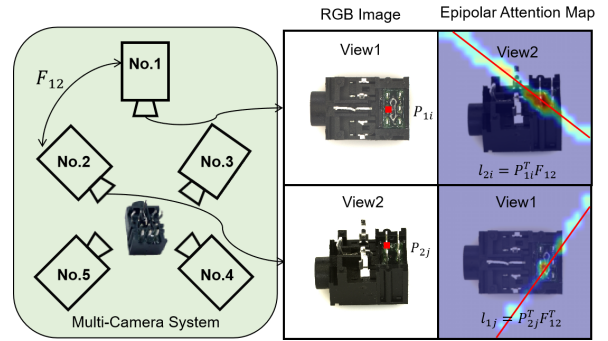


Figure 1. An illustration of epipolar geometry guided attention in a multi-camera system. The corresponding patch of P_{1i} in views lies on the epipolar line $l_{2i} = P_{1i}^T F_{12}$ (red line). Attention map is restricted to the patches on the epipolar line.

els for each viewpoint and perform inference independently, neglecting the correlation between views. This limits the potential of multi-view information, as defects may be subtle in certain perspectives while more pronounced in others. Effectively fusing information across viewpoints could improve anomaly detection by leveraging complementary features, thus improving anomaly prediction at the level of each view respectively and the overall object.

Recent efforts in multi-view anomaly detection have explored feature fusion, cross-view feature alignment, and self-supervised learning [6]. However, many of these methods treat multi-view data similarly to multi-modal inputs, which may not be optimal for structured multi-view camera systems. Inspired by the success of attention-based fusion [7], the Multi-View Adaptive Selection (MVAS) attention mechanism was proposed to enhance multi-view feature aggregation in MVIAD [8]. MVAS partitions feature maps into patches and employs cross-attention to aggregate features from corresponding locations across views. The selection of relevant patches relies on semantic similarity, with cross-view attention learned through reconstruction losses under a reverse distillation framework [9]. The success of MVAS highlights the importance of accurately identifying corresponding regions across views for effective

feature fusion.

Despite these advances, existing methods overlook a fundamental geometric constraint in multi-view camera systems. As illustrated in Fig. 1, industrial inspection setups often have significant overlap between camera views, meaning observations are constrained by epipolar geometry [10]. Specifically, for a pixel p_{1i} in view 1, its corresponding projection in view 2, p_{2i} , must satisfy the epipolar constraint, $p_{1i}^\top F_{12} p_{2i} = 0$, where F_{12} is the fundamental matrix. This suggests that cross-view attention should not rely solely on semantic similarity [8] but could be guided by epipolar geometry to enhance feature correspondence. To this end, we propose an **Epipolar Attention Module (EAM)** for cross-view feature fusion. Given a reference patch in one view, we first identify candidate corresponding patches in other views along the epipolar line. These patches then serve as keys and values in cross-view attention, ensuring feature aggregation is geometrically consistent. We append EAM to the output of regular ViT encoder to fuse features across multiple viewpoints. Our anomaly detection framework is built upon a memory bank based method [11] due to the compatibility with arbitrary encoder architectures, in comparison, distillation-based methods [8, 9, 12] are mostly restricted to CNN architectures. Therefore, our proposed method is referred to as **Multi-View Epipolar Attention Anomaly Detection (MVEAD)** with an overview presented in Fig. 2.

Our experiments in Tab. 3 reveal that EAM is ineffective when the projection layers are not properly initialized. Existing attempts to integrate epipolar geometry into cross-view attention optimizes the projection layers in a fully supervised manner [13]. However, memory-bank-based anomaly detection lacks an explicit objective for training attention projection layers. To address this challenge, we introduce a *multi-center pretraining strategy*, inspired by one-class classification which minimizes feature space volume [14]. Given the complex distribution of normal patterns in industrial images, we extend this idea by introducing multiple cluster centers and reduce the gap between training samples and its closest cluster center. To prevent model collapse, where all features map to a single or few centers, we introduce *synthetic negative samples* tailored to epipolar attention properties as a regularization mechanism. The negative sample synthesis differs from the purely synthesis-based anomaly detection methods [15, 16] in that we focus more on the interaction between different viewpoints for synthesis and use them as regularization. Finally, due to view-dependent defect variations, a single memory bank is suboptimal for multi-view anomaly detection. To improve inference, we use a multi-view memory bank strategy to maintain separate banks for each viewpoint.

We summarize the key contributions of this work as follows:

- We recognize that defects exhibit varying visibility across different viewpoints in a multi-view camera system. While existing methods rely solely on data-driven feature fusion, we propose leveraging epipolar geometry to guide cross-view attention, ensuring more precise feature aggregation.
- We extend the memory bank-based anomaly detection framework, which lacks an explicit training objective, by introducing a multi-center pretraining strategy to optimize the parameters of the epipolar attention module. Additionally, we incorporate consistency-based negative sample synthesis to prevent trivial solutions.
- We validate our approach on the state-of-the-art multi-view industrial anomaly detection dataset, demonstrating its effectiveness while maintaining inference efficiency.

2. Related Work

Industrial Anomaly Detection: Anomaly detection (AD) [17] identifies anomalies in target-class images and localizes anomaly regions. Mainstream AD techniques fall into three categories. Synthesizing-Based Approaches introduce artificial defects to expose models to diverse anomalies. CutPaste [15] relocates patches within an image, while SimpleNet [18] perturbs feature space with Gaussian noise. DRAEM [19] synthesizes anomalies using texture datasets [20], and RealNet [16] improves anomaly realism with diffusion models [21]. Reconstruction-Based Approaches assume models trained on normal data struggle to reconstruct anomalies. AutoEncoders [22], GANs [23], VAEs [24], and diffusion models [16] are commonly used. However, these models may fail if anomalies resemble nominal data or exploit shortcut learning [25]. Recent methods [19, 26, 27] address this by injecting pseudo anomalies or using additional supervision. Embedding-Based Approaches learn feature representations where nominal data cluster compactly, and anomalies deviate. PaDiM [28] models local feature statistics, PatchCore [11] detects anomalies via nearest-neighbor search in a memory bank, and knowledge distillation methods [9] compare outputs from teacher-student networks. Normalizing Flow [29] [30] models feature distributions but incurs high computational costs due to limited downsampling.

Multi-View Deep Learning: Multi-view representation learning has been widely applied across various domains. Early work such as MVCNN [31] pioneered CNN-based multi-view aggregation. In pose estimation, multi-view fusion enhances feature representation [32, 33], with AdaFuse [34] selecting the highest heatmap response along the epipolar line and the Epipolar Transformer [13] leveraging a non-local module [7] for adaptive fusion. For multi-view stereo (MVS) [35], MVSNet [36] introduced cost volume regularization for scene reconstruction, inspiring further refinements in efficiency and depth accuracy [37–39].

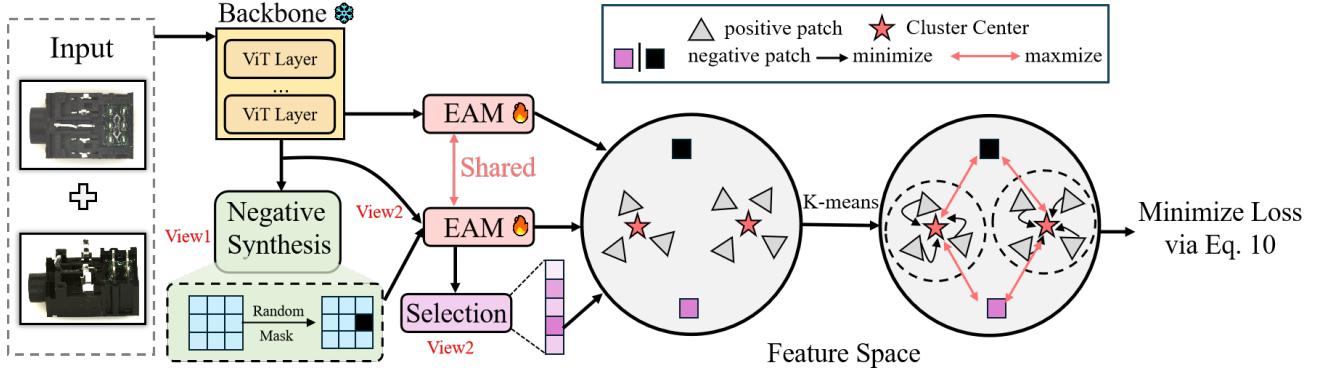


Figure 2. Overview of the proposed multi-center pre-training framework. Multi-view images are processed by a frozen backbone, followed by cross-view fusion via the EAM module to construct a patch-level feature bank. Features from reference view are randomly masked, while other views remain unchanged. In the EAM output, masked patches from the reference view and patches explicitly selected from source views via Eq. (8) serve as negatives, with the loss computed using Eq. (10).

Multi-View Anomaly Detection: Multi-view anomaly detection remains underexplored. Existing works addressing multi-view anomaly detection have studied multiple modality inputs [6, 40], different lightning conditions [41], etc. Industrial anomaly detection from multiple camera viewpoints was less studied due to the lack of valid benchmarks. Real-IAD [5] introduced an initial dataset featuring top-down and side view observations of industrial objects with extensive evaluation of state-of-the-art single-view industrial anomaly detection methods. To exploit complementary information from multiple views, MVAD [8] applied neighborhood attention for feature fusion across views. The attention is computed via semantic similarity, thus lacking explicit geometric constraints. Our method improves upon this by incorporating an epipolar transformer-inspired attention mechanism, leveraging epipolar geometry for more precise and robust multi-view feature aggregation.

3. Methods

3.1. Preliminaries

We formally define the task of multi-view anomaly detection as follows. Each instance consists of images captured from V viewpoints, denoted as $x_i \in \mathbb{R}^{V \times 3 \times H \times W}$. The objective is to predict anomalies at both the instance and pixel levels, identifying defective regions in each view.

Memory Bank-Based Anomaly Detection: We revisit the memory bank-based anomaly detection paradigm. Given a pre-trained encoder network $f(x; \Theta)$, such as a ViT [42], the input image is first patchified into tokens, which are then processed through transformer blocks to extract tokenized features. For an input sample x_i , we denote its tokenized feature on the v -th view as $z_{iv} \in \mathbb{R}^{H \cdot W / P^2 \times D}$, where D , H , W , and P represent the feature channels, input image height, width, and patch size, respectively.

A memory bank $\mathcal{M} = \{m_k\}$ stores representative to-

kenized features for anomaly prediction. Since storing all tokens from normal training data is impractical due to prohibitive memory requirements, core-set selection is typically employed to retain a subset of tokens in \mathcal{M} [11]. Anomalies in a test image are detected at the token level using the following scoring function:

$$s_i = \max_j \min_{m_k \in \mathcal{M}} \|z_{ivj} - m_k\| \quad (1)$$

Cross-View Attention for Multi-View Anomaly Detection: Detecting anomalies using multi-view observations is an emerging topic. Early approaches formulated this task by independently predicting anomalies for each view [5], failing to leverage the strong correlations between views. To exploit cross-view information, [8] introduced a cross-view attention mechanism, aggregating information from supporting views for each reference view.

Specifically, we refer z_i to as a tokenized feature map $z_i \in \mathbb{R}^{V \times H \cdot W / P^2 \times D}$ extracted by a transformer network. The attention mechanism between the reference view z_{ia} and supporting views $\{z_{ib}\}_{b \neq a}$ follows a standard cross-attention formulation, where W_Q , W_K , and W_V are learnable projection matrices,

$$\text{Attn}(z_{ia}) = \text{softmax} \left(\frac{QK^\top}{\sqrt{D}} \right), \quad (2)$$

$$Q = W_Q z_{ia}, \quad K = W_K z_{ib}, \quad V = W_V z_{ib}$$

While cross-view attention improves upon independent predictions, it relies solely on semantic similarity, which can be unreliable for textureless or repetitive patterns. Learning such attention in a purely data-driven manner demands large-scale training data and is prone to errors. To address this, we propose leveraging epipolar geometry as a structural constraint, enhancing both robustness and efficiency in cross-view fusion.

3.2. Epipolar Attention for Multi-View Fusion

Epipolar Geometry: In non-degenerate stereo vision, pixel correspondences between two camera views are governed by epipolar geometry. Given a pixel in view a , denoted as $p_a = [u_a, v_a, 1]^T$, its corresponding projection in view b , $p_b = [u_b, v_b, 1]^T$, must lie on the epipolar line, satisfying the epipolar constraint:

$$p_a^T F_{ab} p_b = 0 \quad (3)$$

where F_{ab} is the fundamental matrix relating the two views. The corresponding epipolar line in view b is parameterized as $l_b = F_{ab}^T p_a$. The fundamental matrix F_{ab} can be efficiently estimated using the eight-point algorithm [10].

Cross-View Attention with Epipolar Constraint: Unlike existing cross-view attention mechanisms that rely solely on feature similarity, we propose incorporating epipolar geometry as a structural prior to guide cross-view attention. Specifically, given a patch in the reference view z_{iaj} , we first determine its center point p_{iaj} using:

$$p_{iaj} = \begin{bmatrix} \left(\left\lfloor \frac{jP}{W} \right\rfloor + 0.5 \right) P \\ \left(j \bmod \frac{W}{P} + 0.5 \right) P \\ 1 \end{bmatrix} \quad (4)$$

Following epipolar geometry, the projection of p_{iaj} in the b -th supporting view lies on the epipolar line parameterized by $(p_{iaj}^T F_{ab}) p_{ibk} = 0$. Any p_{ibk} satisfying this equation could correspond to p_{iaj} . To integrate this prior into cross-view attention, we identify all patches in the supporting view that overlap with the epipolar line. We define a binary mask $M_{ab} \in \{0, 1\}^{H \cdot W / P^2 \times H \cdot W / P^2}$ that dictates the epipolar attention between views a and b , formulated as,

$$M_{ab}[j, k] = \begin{cases} 1, & \text{if } d_{jk} \leq \delta \\ 0, & \text{otherwise} \end{cases} \quad (5)$$

$$\text{where } d_{jk} = \frac{|l_b p_{ibk}|}{\sqrt{(l_b)_1^2 + (l_b)_2^2}}, \quad l_b = p_{iaj}^T F_{ab}$$

The final Epipolar Attention Module (EAM) is formulated as,

$$z_{iaj} = W_O \sum_k M_{ab}[j, k] \cdot \text{Attn}(z_{iaj}) V + z_{iaj},$$

$$\text{Attn}(z_{iaj}) = \frac{\exp(QK^T / \sqrt{D})}{\sum_k \exp(QK_k^T / \sqrt{D}) M_{ab}[j, k]}, \quad (6)$$

$$Q = W_Q z_{iaj}, \quad K = W_K z_{ib}, \quad V = W_V z_{ib}.$$

During pre-training and inference, the EAM module takes the output of the k -th layer of the ViT-like backbone as input, generating the feature for constructing the memory bank while facilitating feature aggregation across all supporting views and leveraging epipolar constraints for improved robustness and efficiency.

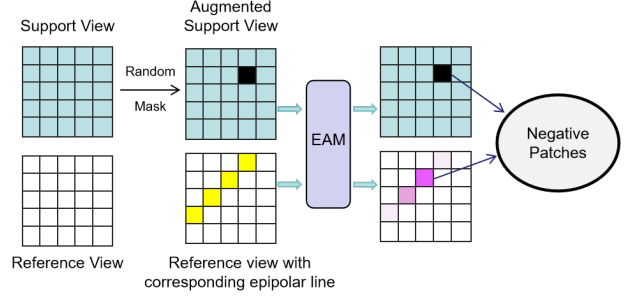


Figure 3. After randomly selecting the support view, a random mask is applied. Following EAM processing, the Top-K patches along the epipolar line corresponding to the masked region in the reference view are selected based on Eq. (8) and used as negative patches along with the masked patch.

3.3. Multi-Center Pre-training

Unlike epipolar transformer [13], where end-to-end training is available to refine linear projection layers, memory bank-based anomaly detection lacks an explicit training objective for optimizing the backbone network. Leaving these projection layers randomly initialized can degrade performance. To address this, we propose a pre-training strategy for optimizing the projection layers in EAM.

Inspired by unsupervised one-class classification, DeepSVDD [14] pre-trains networks by minimizing the volume of a data-enclosing hypersphere with radius $R > 0$ and center $c \in \mathbb{R}^D$. However, a single feature cluster may be insufficient for modeling industrial objects with diverse appearances. Since the inference relies on nearest-neighbor search in the memory bank, a well-distributed set of prototypes should follow a multi-modal distribution. This motivates our multi-center pre-training approach, which preserves multiple feature centers. We maintain K cluster centers $\{c_k \in \mathbb{R}^D\}_{k=1 \dots K}$ in the patch feature space, initializing them via K-Means clustering. During pre-training, patches are iteratively assigned to their closest prototype, and their distances are minimized:

$$\min_{\Theta} \frac{1}{N} \sum_{i,v,j} \|z_{ivj} - m_{k^*}\|, \quad (7)$$

$$s.t. \quad k^* = \arg \min_{m_k \in \mathcal{M}} \|m_k - z_{ivj}\|$$

Multi-View Memory Bank Existing memory bank-based methods primarily target single-view datasets, maintaining a single memory bank for normal sample distributions. In multi-view anomaly detection, significant view-point changes can obscure defect discrimination. To address this, we propose a multi-view memory bank, $\{\mathcal{M}_v\}_{v=1 \dots V}$, where each individual view maintains its own memory representation.

Regularization with Synthesized Negative Samples: Pre-training solely on clean patches risks model collapse, compressing all features into a few trivial representations. To

mitigate this, we introduce negative sample regularization, synthesizing anomalous patches to enforce discriminative learning.

Unlike single-view setups, multi-view anomaly detection requires leveraging cross-view consistency to generate meaningful negative samples. For each sample with V viewpoints, we randomly select one viewpoint as the support view b . Given a reference view a and the support view b , we follow the steps to identify negative patches.

First, we select a patch p_{ibk} in view b and identify corresponding patches in view a using epipolar constraints (Sec. 3.2). We further extract reference view features $Z_{ia} = \{z_{iaj}\}$ and then mask out the support view patch and perform inference again, obtaining updated features $\tilde{Z}_{ia} = \{\tilde{z}_{iaj}\}$. Finally, we identify potential negative patches \mathcal{Z}_{neg} by selecting the top N_k most altered patches,

$$\begin{aligned} \tilde{\mathcal{Z}}_{neg} &= \{\tilde{z}_{iaj}\}_{j=1\dots J^*[1:N_k]} \cup \{\tilde{z}_{ibk}\}, \\ s.t. \quad J^* &= \arg \operatorname{sort}_j \|z_{iaj} - \tilde{z}_{iaj}\|_2 \end{aligned} \quad (8)$$

Negative patches are incorporated into pre-training by penalizing their logarithmic average distance to memory bank cluster centers, preventing them from collapsing into trivial solutions,

$$\mathcal{L}_{neg}(z_{iv}) = - \sum_{\tilde{z}_{ivj} \in \tilde{\mathcal{Z}}_{neg}} \log \left(\frac{1}{|\mathcal{M}_v|} \sum_{m_k \in \mathcal{M}_v} \|\tilde{z}_{ivj} - m_k\|_2 \right) \quad (9)$$

Final Training Objective: Our final loss combines positive and negative patches,

$$\begin{aligned} \min_{\Theta} \sum_{i,v,j} \|z_{ivj} - m_{k^*}\| + \lambda \sum_{i,v} \mathcal{L}_{neg}(z_i), \\ s.t. \quad k^* = \arg \min_{m_k \in \mathcal{M}_v} \|m_k - z_{ivj}\| \end{aligned} \quad (10)$$

Inference: The sample-level anomaly score is determined as the maximum across all views, with each view’s anomaly score being the highest patch-level deviation from the nearest memory bank prototype,

$$s_i = \max_{0 \leq i < v} s_{iv}, \quad s_{iv} = \max_j \min_{m_k \in \mathcal{M}_v} \|z_{ivj} - m_k\| \quad (11)$$

4. Experiments

4.1. Experiment Details

Datasets: To evaluate multi-view industrial anomaly detection, we conduct experiments on Real-IAD [5], a dataset comprising 30 sub-datasets with a total of 150K high-resolution images, each representing a distinct industrial object. For each object, images are captured from five different viewpoints to simulate real-world inspection conditions. Following standard unsupervised anomaly detection protocols, we use only normal samples for training, while test

sets contain both normal and anomalous images with pixel-wise anomaly annotations. Our evaluation includes both single-class and multi-class detection settings. i) Single-class setting: Models are trained and evaluated independently on each object category, ensuring a fair per-category assessment. ii) Multi-class setting: The full dataset is used for pre-training and memory bank construction, enabling evaluation in a broader setting.

Evaluation Metrics: We assess anomaly detection performance at three levels, i.e. image-level, pixel-level, and sample-level. Image-level evaluation measures the model’s ability to distinguish between normal and anomalous instances. Pixel-level evaluation quantifies localization accuracy by assessing pixel-wise anomaly scores. Sample-level evaluation aggregates anomaly scores from multiple viewpoints of the same sample, computing the maximum score across views (as defined in Eq. (11)), providing a more realistic approximation of industrial inspection scenarios. For each level, we report Area Under the Receiver Operating Characteristic Curve (AUROC) and Average Precision (AP) as standard performance metrics.

Implementation Details: Each image is resized to 224×224 without data augmentation, and each sample consists of five different viewpoints. The batch size is set to 8, resulting in 40 images per iteration. We utilize a pretrained DINOv2 [44] network as a frozen image encoder, extracting features from the 7-th layer of the backbone. DINOv2 employs a 14×14 patch size and produces feature embeddings of 768 dimensions. For a fair comparison, we replace the baseline backbone of PatchCore [11] (WideResNet50) with the same DINOv2 model. To train the Epipolar Attention Module, we use the AdamW optimizer [45] with a learning rate of $1e-4$ and a weight decay of $1e-4$ for 50 epochs. The mask threshold δ is set to 1 patch, and the number of cluster centers K is set to 20. The N_k in Eq. (8) is set to 1, while the regularization penalty weight λ for negative sample-based loss in Eq. (10) is set to 0.1. All experiments are conducted on a single NVIDIA A5000 GPU with 24 GB of memory.

4.2. Evaluations on Multi-View Industrial Anomaly Detection

We compared with four state-of-the-art methods. Specifically, UniAD [43] presents a reconstruction based method to simultaneously predict anomaly for all semantic objects. SimpleNet [18] adapts pretrained network to industrial data distribution and introduced a generator and discriminator for anomaly detection. MVAD [8] proposed to fuse feature across multiple views via similarity based cross-view attention. PatchCore [11] is a memory bank based anomaly detection, we extract feature on each view separately for PatchCore.

Sample-Level Evaluation: We first present the evalua-

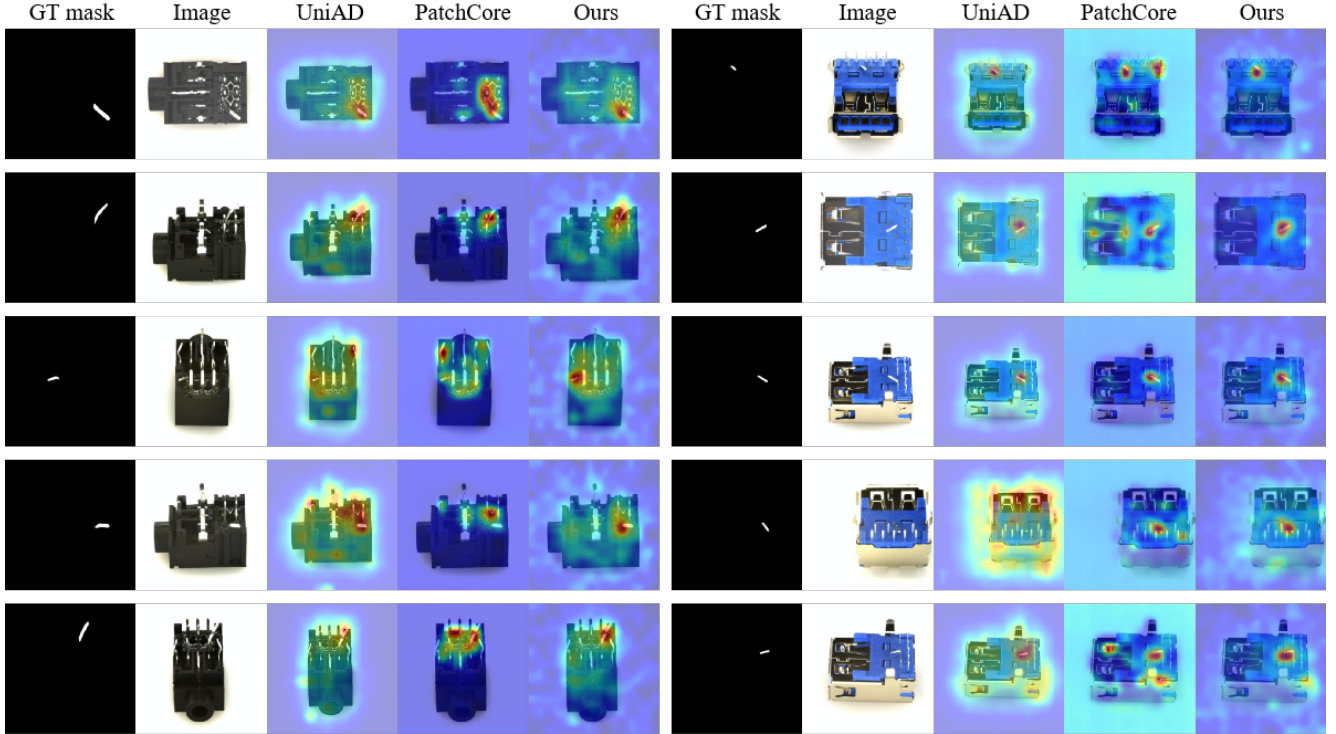


Figure 4. Anomaly segmentation results for two samples from the Real-IAD dataset: the audiojack class (left) and the USB class (right).

tions on sample-level anomaly detection for both single-class and multi-class protocols in Tab. 1. We make the following observations from the results. i) Superior Performance of MVEAD: Our proposed MVEAD consistently outperforms all competing methods across both AUROC and AP metrics. Under the single-class protocol, MVEAD improves upon the state-of-the-art by 1.6% in AUROC and 0.5% in AP. ii) Greater Gains in the Multi-Class Setting: Under the more challenging multi-class protocol, MVEAD achieves an even more pronounced improvement, with 1.8% higher AUROC. Notably, strong baselines such as SimpleNet (94.6% \rightarrow 60.8% AUROC) and MVAD (94.3% \rightarrow 89.0% AUROC) suffer significant performance degradation in this setting, likely due to confusion between different object classes. While UniAD shows slightly better performance in the multi-class protocol, its overall performance lags behind other competitors. iii) Effectiveness of Memory Bank-Based Methods: Methods based on memory banks, such as PatchCore and MVEAD, demonstrate a stronger ability to capture the complex distribution of normal samples, thereby maintaining better performance in the multi-class setting.

Image-Level Evaluation: We further present the evaluations at image-level anomaly detection in Tab. 2 with the following key findings. i) Image-Level Detection is More Challenging: Compared to sample-level evaluations, image-level anomaly detection generally yields lower AUROC and AP scores, as defects may be less noticeable

from certain views, making anomaly identification more difficult. ii) Cross-View Attention Benefits Image-Level Detection: While PatchCore outperforms MVAD at the sample level, MVAD consistently surpasses PatchCore in image-level evaluation, highlighting the benefits of cross-view feature fusion. However, our MVEAD still achieves the best performance across all metrics. The significant improvement over PatchCore (88.1% \rightarrow 91.5% AUROC), which shares a similar inference pipeline, underscores the effectiveness of our epipolar attention module. iii) Lower AP Scores Due to Class Imbalance: We observe relatively lower AP scores in image-level evaluations, likely due to the higher class imbalance—many views may not contain visible anomalies. This suggests that AP should be given more consideration in highly multi-view settings, where class imbalance is more severe than in single-view scenarios.

Qualitative Evaluation: We present qualitative evaluations in Fig. 4. In general, our method is able to better localize the correct anomalous region. In comparison, UniAD produces many false positive predictions forming many local maximums which could severely confuse human understanding. Compared with PatchCore, MVEAD is able to better localize the defects. However, there are some blurry ghost predictions in MVEAD. This might be caused by accidentally fusing anomalous features from other views. This suggests potential areas for improvement in refining cross-view attention mechanisms to mitigate feature leakage.

Ablation Study: We investigate two types of cross-view fu-

Table 1. Comparison of **Sample-level AUROC** and **Sample-level AP** results for our method on Real-IAD dataset with **Single-class/Multi-class setting**.

Category	AUROC					AP				
	UniAD[43]	SimpleNet[18]	MVAD[8]	PatchCore[11]	MVEAD (Ours)	UniAD[43]	SimpleNet[18]	MVAD[8]	PatchCore[11]	MVEAD (Ours)
audiojack	88.4/90.3	93.0/68.3	93.1/91.2	93.0/ 93.2	95.3/92.7	93.4/95.2	96.5/82.4	96.3/94.9	96.5/ 96.6	97.0/96.4
bottle cap	90.8/97.2	99.3/51.2	98.9/ 97.8	95.1/93.9	99.5/93.5	95.2/98.7	99.7/70.4	99.5/ 98.9	97.8/97.3	99.7/97.1
button battery	88.3/95.5	96.1/57.2	93.4/80.0	93.3/94.2	97.0/97.5	91.8/95.1	96.4/75.2	96.4/90.4	95.5/96.8	96.8/97.2
end cap	85.3/87.7	95.1/55.7	91.9/86.6	94.5/90.6	95.6/92.0	92.0/94.2	97.7/73.7	96.1/93.0	97.3/95.3	97.8/95.9
eraser	93.2/90.1	94.3/35.8	91.8/87.2	94.3/91.5	95.8/92.5	96.8/95.3	97.5/61.6	96.3/94.3	97.4/96.1	97.2/ 96.6
fire hood	89.4/85.9	93.5/54.2	90.2/81.8	85.1/82.3	93.8/91.8	94.1/92.9	96.5/69.4	95.1/90.7	92.5/90.6	97.3/95.4
mint	61.0/66.5	86.1/53.1	85.9/68.1	84.6/82.3	87.4/86.5	88.0/89.7	96.7/84.7	96.5/91.0	96.3/95.2	96.9/96.7
mouunts	93.4/98.3	99.5/64.1	99.6/98.8	98.9/98.6	99.1/ 98.9	96.9/99.2	99.7/79.7	99.8/99.5	99.5/99.4	99.5/99.4
pcb	79.4/83.8	91.5/61.2	91.1/ 90.0	91.1/89.2	92.4/88.8	86.7/91.6	95.7/77.2	95.9/ 95.3	95.9/95.1	96.4/95.0
phone battery	91.5/85.4	96.3/62.4	94.2/92.7	94.7/94.3	96.6/96.1	96.1/93.1	98.1/78.4	97.2/96.7	97.4/97.2	98.3/98.1
plastic nut	86.4/84.7	96.1/48.2	97.2/90.8	95.6/94.2	96.4/ 95.2	88.8/89.5	97.5/66.3	98.5/94.7	97.4/ 97.1	97.9/97.0
plastic plug	65.6/80.2	96.0/50.2	94.4/89.1	94.5/92.3	95.4/ 92.8	81.2/90.3	98.2/71.0	97.3/94.6	97.6/96.6	98.0/ 96.8
porcelain doll	65.9/90.1	96.6/80.2	96.2/94.9	97.5/96.2	98.5/97.1	78.4/91.9	98.2/89.1	98.3/97.3	98.5/98.2	99.4/98.6
regulator	52.1/65.7	96.3/49.9	87.7/73.6	97.2/85.0	96.7/91.5	69.8/80.6	98.5/68.1	93.5/86.8	98.6/92.2	98.4/ 95.2
rolled strip base	97.8/98.6	99.8/65.5	99.6/97.7	99.2/97.8	99.7/99.2	99.0/99.3	99.9/80.8	99.8/98.7	99.6/98.8	99.5/99.6
sim card set	93.2/87.3	99.0/77.1	98.2/96.2	98.6/97.5	99.5/99.3	93.6/90.8	99.5/86.7	99.1/97.9	99.4/98.7	99.5/99.7
switch	92.9/91.5	98.6/66.8	96.3/94.9	98.6/ 97.8	98.7/96.7	96.4/96.2	99.4/82.0	98.4/97.6	99.4/98.9	99.4/98.5
tape	94.8/98.2	99.9/54.2	100.0/98.4	99.9/99.2	99.8/ 99.5	97.4/99.0	100.0/73.9	100.0/99.3	100.0/99.6	99.9/ 99.7
terminalblock	82.9/95.7	98.2/75.4	98.6/96.8	98.7/97.9	98.5/ 98.4	92.2/98.2	99.3/87.8	99.4/98.7	99.5/99.2	99.4/ 99.3
toothbrush	94.3/89.8	96.1/71.2	95.8/87.0	97.7/96.0	97.0/ 96.5	96.6/92.9	98.1/83.7	97.0/93.1	98.5/97.7	98.3/97.5
toy	86.3/75.4	93.8/59.0	93.6/86.4	97.0/93.1	97.4/97.5	90.9/85.7	96.9/74.3	96.8/92.3	98.6/95.8	98.6/98.8
toy brick	80.1/78.6	87.1/59.2	80.8/69.4	81.3/76.1	88.3/84.8	85.6/84.3	92.6/73.6	89.7/81.7	90.8/86.1	93.6/91.7
transistor1	96.1/98.4	99.8/66.8	99.8/98.8	98.7/98.2	99.8/98.4	97.7/99.2	99.9/81.6	99.9/99.5	99.3/99.1	99.5/99.2
u block	91.2/94.8	98.7/50.5	98.4/93.0	98.0/ 98.2	98.1/97.3	94.9/97.0	99.4/75.3	99.0/96.1	98.9/ 99.1	98.4/98.3
usb	84.0/79.7	93.9/64.1	96.3/92.1	95.1/ 94.1	95.2/92.7	88.9/88.4	96.1/79.9	97.7/95.9	96.8/ 96.7	96.3/96.0
usb adaptor	78.4/82.9	93.8/48.8	93.3/91.0	94.9/92.6	95.4/93.8	87.7/90.3	97.1/70.4	96.5/95.5	97.8/96.7	98.1/97.2
vepill	79.8/80.7	96.8/64.5	95.9/88.2	98.2/96.2	97.8/ 97.1	88.9/89.9	98.4/78.7	98.1/94.2	99.2/98.2	98.9/ 98.5
wooden beads	78.5/77.3	92.1/59.5	92.7/82.2	93.9/90.8	95.7/94.4	90.1/90.1	97.0/81.3	97.2/92.7	97.7/96.2	98.4/98.0
woodstick	81.8/84.0	80.3/58.2	85.0/76.8	84.2/79.4	86.0/84.7	87.3/90.7	90.5/72.7	92.5/87.5	92.2/89.6	92.9/92.7
zipper	94.6/97.8	99.6/91.9	99.6/ 99.9	99.8/99.8	100.0/99.9	96.2/98.6	99.9/96.0	99.8/99.9	99.9/99.9	99.9/99.9
Average	84.6/87.1	94.6/60.8	94.3/89.0	94.8/92.8	96.2/94.6	91.1/92.9	97.3/77.5	97.3/94.6	97.5/96.5	98.0/97.3

sion methods (Cross-View Attn.), including semantic similarity based multi-view adaptive selection (MVAS) proposed by [8] and our epipolar attention module (EAM). We further investigate different pretraining strategies. These include directly copying the projection layer from the 8-th layer of the backbone which adopts to the output of the 7-th layer in the backbone (**Copy**), reducing volume in feature space (DeepSVDD [14]), our proposed multi-center pretraining (**MCP**) and additionally included the negative samples for regularization (**MCP+Reg**). Finally, we also include the multiview memory bank (**MultiView MB**).

We make the following observations from the results in Tab. 3. i) Cross-view attention must be properly trained to be effective. For both MVAS and EAM, directly copying the weights yields inferior results than without any cross-view fusion. ii) Reducing data volume in the features space (DeepSVDD) provides signal to train the projection layers and improves upon without training, however is still behind the baseline. iii) Multi-center pretraining can further boost the performance, suggesting encouraging local clusters in feature space is conducive to memory bank based anomaly inference. iv) Both multi-view memory bank and negative sample synthesis as regularization are complementary to the overall method.

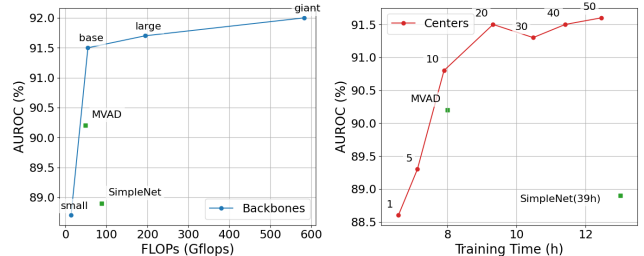


Figure 5. Computation overhead for different backbone sizes (DINOv2-small/base/large/giant) and center numbers K .

4.3. Additional Studies

We demonstrate that overall performance remains relatively unaffected by computational overhead. As shown in the left subfigure of Fig. 5, DINOv2-small exhibits low computational cost but achieves only 88.7% AUROC, suggesting that its limited hidden dimensions fail to capture fine-grained anomalies. In contrast, DINOv2-giant attains the highest AUROC (92.0%) but incurs a substantial computational burden (over 600 GFlops). The DINOv2 base model strikes a favorable balance, achieving 91.5% AUROC while maintaining significantly lower FLOPs than its larger coun-

Table 2. Comparison of **Image-level AUROC** and **Image-level AP** results for our method on Real-IAD dataset with **Single-class/Multi-class setting**.

Category	AUROC					AP				
	UniAD[43]	SimpleNet[18]	MVAD[8]	PatchCore[11]	Ours	UniAD[43]	SimpleNet[18]	MVAD[8]	PatchCore[11]	Ours
audiojack	78.7/81.4	88.4/58.4	86.9/80.3	86.5/86.3	90.1/87.7	60.8/76.6	84.4/44.2	82.5/72.8	82.8/82.7	87.5/84.1
bottle cap	85.6/ 92.5	91.1/54.1	95.6/92.4	93.7/88.2	95.1/87.8	82.6/ 91.7	88.6/47.6	95.4/90.9	93.3/89.5	94.2/88.1
button battery	65.9/75.9	88.4/52.5	90.8/76.6	86.8/88.3	91.2/90.9	71.9/81.6	89.9/60.5	92.1/83.2	89.5/ 90.7	94.4/90.7
end cap	80.6/80.9	83.7/51.6	85.8/79.4	84.8/81.0	86.9/81.3	84.4/86.1	88.4/60.8	88.8/84.6	88.1/86.1	88.9/86.2
eraser	87.9/90.3	91.6/46.4	91.2/88.6	92.5/90.0	92.9/90.6	82.4/ 89.2	90.1/39.1	89.2/87.2	90.4/88.7	90.4/88.6
fire hood	79.0/80.6	81.7/58.1	84.6/78.6	80.1/80.3	87.5/87.0	72.3/74.8	74.1/41.9	77.2/71.8	75.3/73.6	83.6/80.1
mint	64.5/67.0	77.0/52.4	79.5/68.9	76.5/75.3	82.3/76.4	63.8/66.6	78.5/50.3	80.7/70.2	78.1/75.4	82.0/76.9
mounts	84.1/87.6	88.2/58.7	87.9/ 89.5	86.8/87.2	88.0/84.8	71.2/77.3	79.1/48.1	75.6/ 81.5	74.6/77.8	76.3/72.9
pcb	84.0/81.0	89.3/54.5	91.3/87.7	86.3/83.8	91.3/84.9	89.2/88.2	93.5/66.0	94.6/92.5	91.1/90.6	94.4/91.5
phone battery	83.7/83.6	86.8/51.6	92.5/ 90.6	91.6/89.3	93.4/89.7	75.9/80.0	81.9/43.8	90.7/ 89.1	88.6/84.8	94.2/86.3
plastic nut	78.7/80.0	89.8/59.2	91.3/84.9	89.4/ 86.2	91.5/84.8	64.7/69.2	83.1/40.3	85.7/77.2	82.6/ 79.8	85.4/77.5
plastic plug	70.7/81.4	87.5/48.2	89.7/85.2	86.1/83.9	87.8/84.2	59.9/75.9	83.7/38.4	87.2/80.1	81.9/ 80.4	79.4/78.0
porcelain doll	68.3/85.1	85.4/66.3	87.8/ 89.2	80.3/85.2	89.8/85.3	53.9/75.2	76.8/54.5	81.5/ 83.4	72.4/79.9	83.3/76.2
regulator	46.8/56.9	81.7/50.5	85.2/66.6	80.0/73.6	85.3/73.8	26.4/41.5	68.3/29.0	75.4/55.4	65.6/ 63.8	59.4/58.3
rolled strip base	97.3/ 98.7	99.5/59.0	99.4/96.9	98.8/97.2	98.7/98.4	98.6/ 99.3	99.7/75.7	99.7/98.2	99.4/98.5	99.2/99.1
sim card set	91.9/89.7	95.2/63.1	96.2/94.1	93.7/95.1	97.7/96.4	90.3/90.3	94.8/69.7	96.7/94.9	94.3/94.8	97.5/96.8
switch	89.3/85.5	95.2/62.2	93.1/89.1	93.9/ 91.2	94.6/88.1	91.3/88.6	96.2/66.8	94.8/91.6	93.6/ 93.2	95.3/91.6
tape	95.1/ 97.2	96.8/49.9	98.1/96.8	97.3/95.6	97.5/96.0	93.2/ 96.2	95.2/41.1	97.4/96.1	93.9/93.2	95.6/94.0
terminalblock	84.4/87.5	94.7/59.8	97.3/93.5	97.0/93.0	97.2/ 93.7	85.8/89.1	95.1/64.7	97.6/94.4	97.5/95.1	97.6/95.4
toothbrush	84.9/78.4	85.8/65.9	85.5/84.8	82.1/ 86.5	87.8/85.7	85.4/80.1	87.1/70.0	84.2/86.7	86.4/ 87.8	86.9/86.1
toy	79.7/68.4	83.5/57.8	86.5/79.1	85.2/83.9	89.4/85.6	82.3/75.1	87.6/64.4	90.2/84.2	85.1/ 87.8	93.3/87.6
toy brick	80.0/77.0	81.8/58.3	77.9/66.4	75.6/77.2	83.5/81.6	73.9/71.1	78.8/49.7	73.6/58.8	72.1/71.7	76.9/ 75.5
transistor1	95.8/93.7	97.4/62.2	97.9/94.3	96.5/ 94.7	93.7/94.6	96.6/95.9	98.1/69.2	98.4/96.0	94.6/96.1	96.6/ 96.2
u block	85.4/88.8	90.2/62.4	93.1/89.1	91.8/89.1	93.2/91.5	76.7/84.2	82.8/48.4	90.2/84.0	90.3/86.2	93.5/88.0
usb	84.5/78.7	90.3/57.0	92.8/90.1	89.1/88.8	92.7/87.9	82.9/79.4	90.0/55.3	92.1/90.5	86.3/88.9	91.5/87.6
usb adaptor	78.3/76.8	82.3/47.5	83.8/78.1	81.7/79.0	87.4/80.2	70.3/71.3	78.0/38.4	78.7/72.4	74.1/73.2	82.8/74.4
vepill	83.7/87.1	90.3/59.0	90.8/83.7	89.8/89.0	94.5/90.5	81.9/84.0	88.8/48.7	90.1/80.9	88.8/ 87.9	92.7/87.7
wooden beads	82.8/78.4	86.1/55.1	89.5/84.3	90.1/86.9	94.6/90.3	81.5/77.2	84.7/52.0	88.9/83.1	89.3/86.5	91.3/89.4
woodstick	79.7/80.8	78.3/58.2	85.7/78.0	84.1/81.0	86.6/86.0	70.4/72.6	70.3/35.6	77.9/65.3	74.4/68.9	77.0/ 74.4
zipper	97.5/98.2	98.7/77.2	99.4/98.9	99.1/99.0	99.3/ 99.1	98.4/98.9	99.2/86.7	99.6/99.4	99.4/99.4	99.6/99.5
Average	81.6/83.0	88.9/57.2	90.2/85.2	88.1/86.8	91.5/87.8	77.3/80.9	87.4/53.4	88.2/83.2	85.6/85.1	88.7/85.3

Table 3. Ablation study on cross-view fusion methods and pre-training strategies, evaluated by Image-AUROC (%).

Cross-View Attn.	Pretrain.	MultiView MB	Results
-	-	-	88.1
MVAS [8]	Copy	-	82.5
MVAS [8]	DeepSVDD [14]	-	85.9
MVAS [8]	MCP	-	87.7
MVAS [8]	MCP+Reg	-	88.6
EAM	Copy	-	84.9
EAM	DeepSVDD [14]	-	86.8
EAM	MCP	-	89.6
EAM	MCP+Reg	-	90.9
EAM	MCP+Reg	✓	91.5

terpart. In comparison, SimpleNet and MVAD are both below the Pareto frontier established by our method.

We also analyze the impact of the number of cluster centers K in \mathcal{M} on performance and inference overhead. As shown in the right subfigure of Fig. 5, increasing K generally improves AUROC but extends training time. A single center yields an AUROC of 88.6% with the shortest training time (6.58 hours), while increasing K to 20 boosts AUROC to 91.5% at the cost of a longer training duration (9.32 hours). However, beyond $K = 20$, AUROC saturates despite the rising computational burden, indicating that 20

centers sufficiently model the patch feature distribution. In comparison, MVAD incurs a similar training cost but yields inferior performance, while SimpleNet requires five times the training cost and performs even worse.

5. Conclusion

We explored improving the efficacy of multi-view anomaly detection by introducing cross-view attention guided by epipolar geometry. Using the fundamental matrix, we localize potential patches in the support view based on a given patch in the reference view. A cross-view attention (EAM) is defined only on the potential patches to eliminate the impact from irrelevant ones. Inspired by the memory bank-based anomaly detection method, we propose a multi-center pre-training strategy. Negative samples are synthesized to regularize the pre-training. Evaluations on Real-IAD dataset demonstrate the effectiveness, achieving superior performance in both single-view and sample-wise anomaly prediction.

References

- [1] Jiaqi Liu, Guoyang Xie, Jinbao Wang, Shangnian Li, Chengjie Wang, Feng Zheng, and Yaochu Jin. Deep industrial image anomaly detection: A survey. *Machine Intelligence Research*, 2024. 1
- [2] Guoyang Xie, Jinbao Wang, Jiaqi Liu, Jiayi Lyu, Yong Liu, Chengjie Wang, Feng Zheng, and Yaochu Jin. Im-riad: Industrial image anomaly detection benchmark in manufacturing. *IEEE Transactions on Cybernetics*, 2024. 1
- [3] Paul Bergmann, Michael Fauser, David Sattlegger, and Carsten Steger. Mvtec ad—a comprehensive real-world dataset for unsupervised anomaly detection. In *IEEE/CVF Conference on Computer Vision and Pattern Recognition*, 2019. 1
- [4] Yang Zou, Jongheon Jeong, Latha Pemula, Dongqing Zhang, and Onkar Dabeer. Spot-the-difference self-supervised pre-training for anomaly detection and segmentation. In *European Conference on Computer Vision*, 2022. 1
- [5] Chengjie Wang, Wenbing Zhu, Bin-Bin Gao, Zhenye Gan, Jiangning Zhang, Zhihao Gu, Shuguang Qian, Mingang Chen, and Lizhuang Ma. Real-riad: A real-world multi-view dataset for benchmarking versatile industrial anomaly detection. In *IEEE/CVF Conference on Computer Vision and Pattern Recognition*, 2024. 1, 3, 5
- [6] Siqi Wang, Jiyuan Liu, Guang Yu, Xinwang Liu, Sihang Zhou, En Zhu, Yuexiang Yang, Jianping Yin, and Wenjing Yang. Multiview deep anomaly detection: A systematic exploration. *IEEE Transactions on Neural Networks and Learning Systems*, 2022. 1, 3
- [7] Xiaolong Wang, Ross Girshick, Abhinav Gupta, and Kaiming He. Non-local neural networks. In *IEEE/CVF Conference on Computer Vision and Pattern Recognition*, 2018. 1, 2
- [8] Haoyang He, Jiangning Zhang, Guanzhong Tian, Chengjie Wang, and Lei Xie. Learning multi-view anomaly detection. *arXiv preprint arXiv:2407.11935*, 2024. 1, 2, 3, 5, 7, 8
- [9] Hanqiu Deng and Xingyu Li. Anomaly detection via reverse distillation from one-class embedding. In *IEEE/CVF Conference on Computer Vision and Pattern Recognition*, 2022. 1, 2
- [10] Richard Hartley and Andrew Zisserman. *Multiple view geometry in computer vision*. Cambridge university press, 2003. 2, 4
- [11] Karsten Roth, Latha Pemula, Joaquin Zepeda, Bernhard Schölkopf, Thomas Brox, and Peter Gehler. Towards total recall in industrial anomaly detection. In *IEEE/CVF Conference on Computer Vision and Pattern Recognition*, 2022. 2, 3, 5, 7, 8
- [12] Tran Dinh Tien, Anh Tuan Nguyen, Nguyen Hoang Tran, Ta Duc Huy, Soan Duong, Chanh D Tr Nguyen, and Steven QH Truong. Revisiting reverse distillation for anomaly detection. In *IEEE/CVF Conference on Computer Vision and Pattern Recognition*, 2023. 2
- [13] Yihui He, Rui Yan, Katerina Fragkiadaki, and Shoubo Yu. Epipolar transformers. In *IEEE/CVF Conference on Computer Vision and Pattern Recognition*, 2020. 2, 4
- [14] Lukas Ruff, Robert Vandermeulen, Nico Goernitz, Lucas Deecke, Shoaib Ahmed Siddiqui, Alexander Binder, Emmanuel Müller, and Marius Kloft. Deep one-class classification. In *International Conference on Machine Learning*, 2018. 2, 4, 7, 8
- [15] Chun-Liang Li, Kihyuk Sohn, Jinsung Yoon, and Tomas Pfister. Cutpaste: Self-supervised learning for anomaly detection and localization. In *IEEE/CVF Conference on Computer Vision and Pattern Recognition*, 2021. 2
- [16] Ximiao Zhang, Min Xu, and Xiuzhuang Zhou. Realnet: A feature selection network with realistic synthetic anomaly for anomaly detection. In *IEEE/CVF Conference on Computer Vision and Pattern Recognition*, 2024. 2
- [17] Yunkang Cao, Xiaohao Xu, Jiangning Zhang, Yuqi Cheng, Xiaonan Huang, Guansong Pang, and Weiming Shen. A survey on visual anomaly detection: Challenge, approach, and prospect. *arXiv preprint arXiv:2401.16402*, 2024. 2
- [18] Zhikang Liu, Yiming Zhou, Yuansheng Xu, and Zilei Wang. Simplenet: A simple network for image anomaly detection and localization. In *IEEE/CVF Conference on Computer Vision and Pattern Recognition*, 2023. 2, 5, 7, 8
- [19] Vitjan Zavrtanik, Matej Kristan, and Danijel Skočaj. Draem—a discriminatively trained reconstruction embedding for surface anomaly detection. In *IEEE/CVF International Conference on Computer Vision*, 2021. 2
- [20] Mircea Cimpoi, Subhransu Maji, Iasonas Kokkinos, Sammy Mohamed, and Andrea Vedaldi. Describing textures in the wild. In *IEEE/CVF Conference on Computer Vision and Pattern Recognition*, 2014. 2
- [21] Jonathan Ho, Ajay Jain, and Pieter Abbeel. Denoising diffusion probabilistic models. *Advances in Neural Information Processing Systems*, 2020. 2
- [22] Samet Akcay, Amir Atapour-Abarghouei, and Toby P Breckon. Ganomaly: Semi-supervised anomaly detection via adversarial training. 2019. 2
- [23] Thomas Schlegl, Philipp Seeböck, Sebastian M Waldstein, Georg Langs, and Ursula Schmidt-Erfurth. f-anogan: Fast unsupervised anomaly detection with generative adversarial networks. *Medical image analysis*, 2019. 2
- [24] Jinwon An and Sungzoon Cho. Variational autoencoder based anomaly detection using reconstruction probability. *Special lecture on IE*, 2015. 2
- [25] Vitjan Zavrtanik, Matej Kristan, and Danijel Skočaj. Reconstruction by inpainting for visual anomaly detection. *Pattern Recognition*, 2021. 2
- [26] Anne-Sophie Collin and Christophe De Vleeschouwer. Improved anomaly detection by training an autoencoder with skip connections on images corrupted with stain-shaped noise. 2021. 2
- [27] Jingyi Liao, Xun Xu, Manh Cuong Nguyen, Adam Goodge, and Chuan Sheng Foo. Coft-ad: Contrastive fine-tuning for few-shot anomaly detection. *IEEE Transactions on Image Processing*, 2024. 2
- [28] Thomas Defard, Aleksandr Setkov, Angélique Loesch, and Romaric Audigier. Padim: a patch distribution modeling framework for anomaly detection and localization. 2021. 2

- [29] Ivan Kobyzev, Simon JD Prince, and Marcus A Brubaker. Normalizing flows: An introduction and review of current methods. *IEEE Transactions on Pattern analysis and Machine Intelligence*, 2020. 2
- [30] Marco Rudolph, Bastian Wandt, and Bodo Rosenhahn. Same same but different: Semi-supervised defect detection with normalizing flows. In *IEEE/CVF Winter Conference on Applications of Computer Vision*, 2021. 2
- [31] Hang Su, Subhransu Maji, Evangelos Kalogerakis, and Erik Learned-Miller. Multi-view convolutional neural networks for 3d shape recognition. In *IEEE International Conference on Computer Vision*, 2015. 2
- [32] Haibo Qiu, Chunyu Wang, Jingdong Wang, Naiyan Wang, and Wenjun Zeng. Cross view fusion for 3d human pose estimation. In *IEEE/CVF International Conference on Computer Vision*, 2019. 2
- [33] Haoyu Ma, Zhe Wang, Yifei Chen, Deying Kong, Liangjian Chen, Xingwei Liu, Xiangyi Yan, Hao Tang, and Xiaohui Xie. Ppt: token-pruned pose transformer for monocular and multi-view human pose estimation. In *European Conference on Computer Vision*, 2022. 2
- [34] Zhe Zhang, Chunyu Wang, Weichao Qiu, Wenhui Qin, and Wenjun Zeng. Adafuse: Adaptive multiview fusion for accurate human pose estimation in the wild. *International Journal of Computer Vision*, 2021. 2
- [35] Yasutaka Furukawa, Carlos Hernández, et al. Multi-view stereo: A tutorial. *Foundations and trends® in Computer Graphics and Vision*, 2015. 2
- [36] Xiaodong Gu, Zhiwen Fan, Siyu Zhu, Zuozhuo Dai, Feitong Tan, and Ping Tan. Cascade cost volume for high-resolution multi-view stereo and stereo matching. In *IEEE/CVF Conference on Computer Vision and Pattern Recognition*, 2020. 2
- [37] Xiang-Rong Sheng, De-Chuan Zhan, Su Lu, and Yuan Jiang. Multi-view anomaly detection: Neighborhood in locality matters. In *AAAI Conference on Artificial Intelligence*, 2019. 2
- [38] Qingshan Xu and Wenbing Tao. Pvsnet: Pixelwise visibility-aware multi-view stereo network. *arXiv preprint arXiv:2007.07714*, 2020.
- [39] Fangjinhua Wang, Silvano Galliani, Christoph Vogel, Pablo Speciale, and Marc Pollefeys. Patchmatchnet: Learned multi-view patchmatch stereo. In *IEEE/CVF Conference on Computer Vision and Pattern Recognition*, 2021. 2
- [40] Zhen Wang and Chao Lan. Towards a hierarchical bayesian model of multi-view anomaly detection. In *International Joint Conference on Artificial Intelligence*, 2020. 3
- [41] Chieh Liu, Yu-Min Chu, Ting-I Hsieh, Hwann-Tzong Chen, and Tyng-Luh Liu. Learning diffusion models for multi-view anomaly detection. In *European Conference on Computer Vision*, 2024. 3
- [42] Alexey Dosovitskiy, Lucas Beyer, Alexander Kolesnikov, Dirk Weissenborn, Xiaohua Zhai, Thomas Unterthiner, Mostafa Dehghani, Matthias Minderer, Georg Heigold, Sylvain Gelly, et al. An image is worth 16x16 words: Transformers for image recognition at scale. *arXiv preprint arXiv:2010.11929*, 2020. 3
- [43] Zhiyuan You, Lei Cui, Yujun Shen, Kai Yang, Xin Lu, Yu Zheng, and Xinyi Le. A unified model for multi-class anomaly detection. *Advances in Neural Information Processing Systems*, 2022. 5, 7, 8
- [44] Maxime Oquab, Timothée Darcet, Théo Moutakanni, Huy Vo, Marc Szafraniec, Vasil Khalidov, Pierre Fernandez, Daniel Haziza, Francisco Massa, Alaaeldin El-Nouby, et al. Dinov2: Learning robust visual features without supervision. *arXiv preprint arXiv:2304.07193*, 2023. 5
- [45] Ilya Loshchilov and Frank Hutter. Decoupled weight decay regularization. *arXiv preprint arXiv:1711.05101*, 2017. 5